Article

Present-day North Atlantic salinity constrains future warming of the Northern Hemisphere

In-Hong Park [1], Sang-Wook Yeh [1] ✉, Wenju Cai [2,3], Guojian Wang [2,3], Seung-Ki Min [4,5] & Sang-Ki Lee [6]

Earth system models exhibit considerable intermodel spread in Atlantic Meridional Overturning Circulation intensity and its carbon uptake, resulting in great uncertainty in future climate. Here we show that present-day sea surface salinity (SSS) in the North Atlantic subpolar region modulates anthropogenic carbon uptake in the North Atlantic, and thus can be used to constrain future warming. Specifically, models that generate a present-day higher SSS in the North Atlantic subpolar region generate a greater uptake of anthropogenic carbon in the future, suppressing the greenhouse effect and resulting in slower warming, and vice versa in models with a present-day lower SSS. Emergent constraints based on the observed SSS greatly reduce the uncertainty of the Northern Hemisphere surface temperature warming and accumulative carbon uptake by about 30% and 53%, respectively, by the end of the twenty-first century under the Shared Socioeconomic Pathways 5–8.5 scenario.

The North Atlantic (NA), where the Atlantic Meridional Overturning Circulation (AMOC) transports both heat and carbon from the tropics, regulates global mean surface temperature and its variability in the present climate[1,2]. A substantial decline of the AMOC is expected under future global warming, weakening ocean heat transport along with increased freshwater flux into the NA[3–5]. The associated oceanic and atmospheric circulation changes include a shift in the Intertropical Convergence Zone, due to enhanced interhemispheric asymmetries in energy fluxes on the top of the atmosphere as well as in ocean heat uptake[6,7]. The NA is a hotspot for affecting global weather and climate[8,9].

The NA covers only 15% of the global ocean surface but accounts for approximately 25% of the anthropogenic carbon (hereafter referred to as carbon) inventory of the world's oceans[10–12]. The amount of carbon uptake in the NA is closely related to AMOC intensity due to the ocean mixing that modulates the solubility and subduction of carbon

from the surface to the deep ocean[13–15]. Greater absorption of carbon by the NA from the atmosphere could delay global warming[16–19]. However, there is a large intermodel spread of NA carbon uptake among Earth system models (ESMs), which is partly due to a large intermodel spread of AMOC intensity[20,21]. Consequently, projection of future global warming is uncertain. Therefore, reducing the uncertainties in carbon uptake in the NA would greatly reduce the uncertainty of future global climate projections, including sea level rise, sea-ice retreat and extreme climate events[22–27].

To reduce the uncertainty in carbon uptake in the NA and its associated Northern Hemisphere (NH) surface warming, here we develop an emergent constraint using the present-day sea surface salinity (SSS), which is derived based on a long-term period of hydrographic data with low observational uncertainties[22,28]. SSS is often used to investigate or represent upper ocean circulations because of its relationship with

[1]Department of Marine Science and Convergence Engineering, Hanyang University, ERICA, Ansan, South Korea. [2]Center for Southern Hemisphere Oceans Research (CSHOR), CSIRO Oceans and Atmosphere, Hobart, Tasmania, Australia. [3]Key Laboratory of Physical Oceanography, Institute for Advanced Ocean Studies, Ocean University of China, Qingdao, China. [4]Division of Environmental Science and Engineering, Pohang University of Science and Technology, Pohang, Republic of Korea. [5]Institute for Convergence Research and Education in Advanced Technology, Yonsei University, Incheon, South Korea. [6]NOAA Atlantic Oceanographic and Meteorological Laboratory, Miami, FL, USA. ✉e-mail: swyeh@hanyang.ac.kr
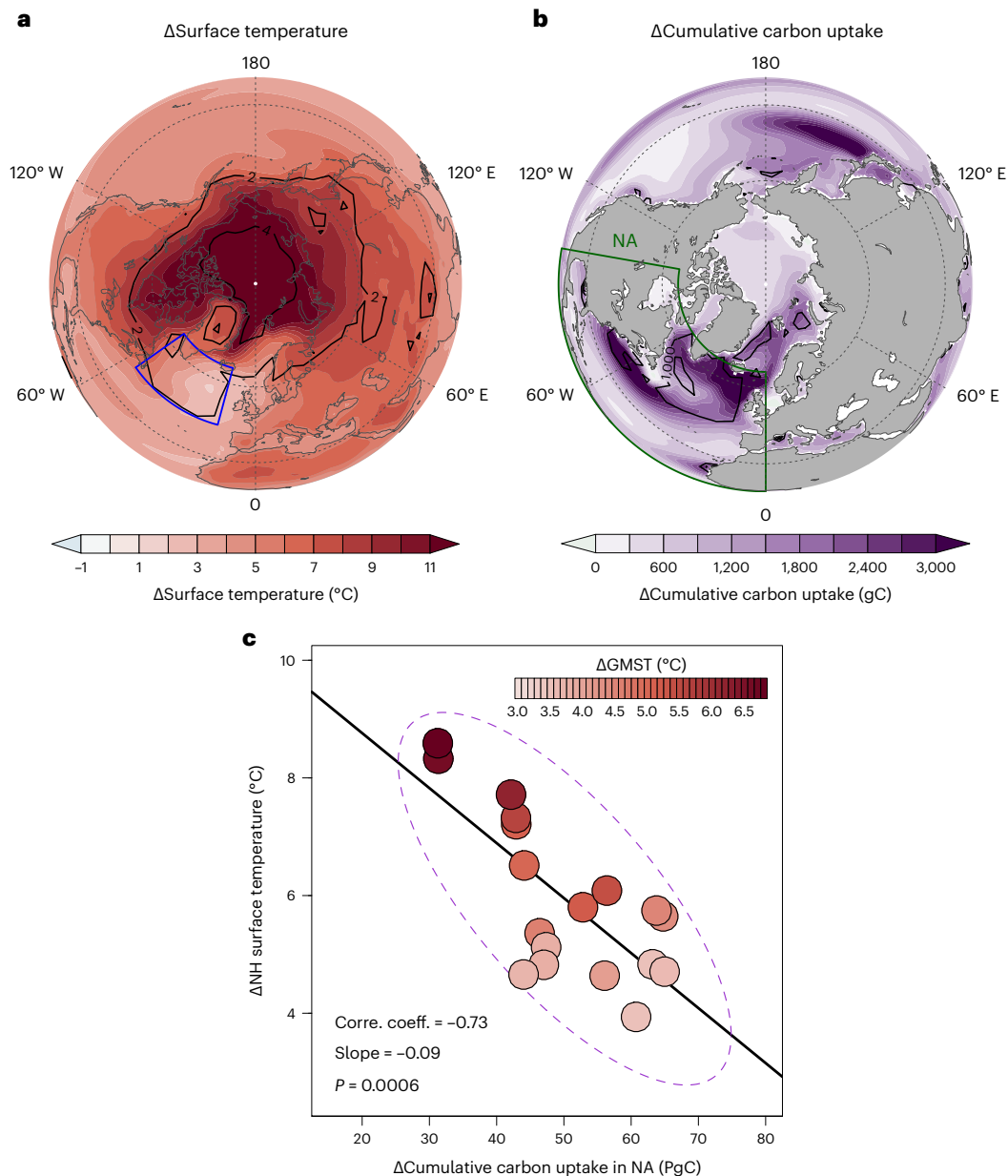
Fig. 1 | Projections of future NH climate under a high-emission scenario.
a,b, Future (2071–2100) changes relative to the pre-industrial period (1850–1900) from 18 CMIP6 ESMs under SSP5–8.5 simulation of surface temperature (**a**) and cumulative carbon uptake (**b**). The NA subpolar region is denoted by a blue outline in **a** and the NA domain is denoted by a green outline in **b**. Contours indicate an intermodel one standard deviation (s.d.) of future changes among ESMs. **c**, Future cumulative carbon uptake in the NA versus future surface temperature changes in the NH. Shadings show the future changes of global mean surface temperature and its correlation coefficient with cumulative carbon uptake in the NA is −0.70, which is slightly smaller than that with the NH surface temperature (*r* = −0.73). The purple dashed ellipse is calculated based on the multivariate normal distribution with 5–95% ranges. Correlation coefficient (Corre. coeff.), slope and *P* value determined by a two-sided Student's *t*-test are also provided with a regression line (black solid line).

ocean density and hence its ability to affect the stability and vertical stratification of the water column[29–31]. In particular, SSS in the NA subpolar region is a well-known proxy for the AMOC because it reflects the AMOC-induced transport of warm and salty water from the subtropical NA[32–35]. We find that the present-day SSS in the NA subpolar region is a reliable indicator of AMOC strength and thus constrains the amount of NA carbon uptake in future climate and NH surface warming in ESMs.

Relationship between carbon uptake and warming

Figure 1 displays changes in surface temperature and cumulative carbon uptake amount in the NH during 2071–2100 compared with pre-industrial climate (1850–1900) as projected by 18 ESMs participating in Phase 6 of the Coupled Model Intercomparison (CMIP6) under

the Shared Socioeconomic Pathways 5–8.5 (SSP5–8.5) simulations (Extended Data Table 1).

The spatial distribution of future multimodel mean surface temperature changes is characterized by the strongest warming in the high latitudes of the NH, with a distinct weak warming in the NA subpolar region (outlined in Fig. 1a), a phenomenon known as the 'warming hole'[36] (Fig. 1a). These regions, including the NA subpolar and Arctic regions, also have a large intermodel uncertainty (Methods) due to either model bias or internal variability (Fig. 1a). Cumulative carbon uptake in the future is mainly concentrated in the NA with a large intermodel uncertainty (Fig. 1b)[15,37]. The projected multimodel mean NH surface warming from 1850–1900 to 2071–2100 is 5.9 ± 1.4 °C. An intermodel uncertainty (that is, ±1.4 °C) is defined as one standard
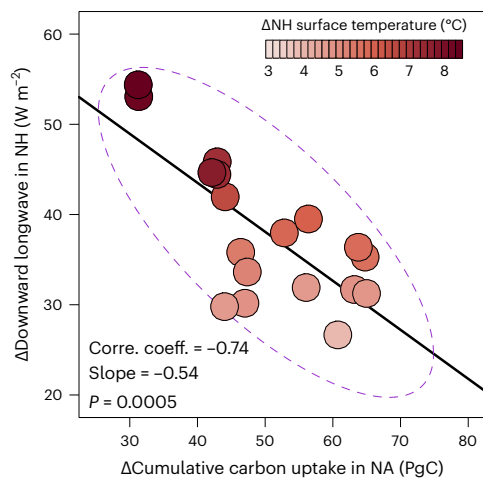
Fig. 2 | Intermodel difference in the greenhouse effect response due to cumulative carbon uptake in the NA among CMIP6 models. Downward longwave changes in the NH against cumulative carbon uptake in the NA among ESMs. Shadings illustrate corresponding NH surface temperature change. The purple dashed ellipse is calculated based on the multivariate normal distribution with 5–95% ranges. Correlation coefficient (Corre. coeff.), slope and *P* value determined by a two-sided Student's *t*-test are also provided with a regression line (black solid line).

deviation of the projected NH surface warming across CMIP6 ESMs. The projected multimodel mean of cumulative NA carbon uptake amount is 50.1 ± 10.7 PgC (Extended Data Fig. 1a). In CMIP Phase 5 (CMIP5) ESMs, the projected NH surface warming and cumulative NA carbon uptake amount are somewhat lower than those in CMIP6 ESMs, at 5.2 ± 1.0 °C and 47.6 ± 11.1 g PgC, respectively (Extended Data Fig. 1b). While CMIP6 ESMs have improved in simulating observed decadal fluctuations of sea surface temperature (SST) in the NA subpolar region compared with CMIP5 ESMs[38], the ranges of intermodel uncertainty in CMIP5 and CMIP6 ESMs are similar (Extended Data Fig. 1).

Changes in NH surface temperature are statistically significantly and negatively correlated with cumulative NA carbon uptake (correlation coefficient, $r = -0.73$) among CMIP6 ESMs (Fig. 1c). Thus, ESMs with a larger NA carbon uptake systematically project a weaker future surface warming in the globe, and more so in the NH, compared with ESMs with a smaller NA carbon uptake. This robust intermodel relationship can be explained by a reduction in the greenhouse effect in models with a larger uptake of carbon from the atmosphere in the NA (Fig. 2). More specifically, a greater cumulative NA carbon uptake decreases the concentration of GHG in the atmosphere, which in turn leads to lower downward longwave radiation (Extended Data Fig. 2). In other words, a larger NA carbon uptake leads to a smaller increase in the downward longwave radiation in the NH, resulting in less surface warming of the NH (Fig. 2). Although the carbon uptake is confined to the NA, its influence reaches the whole NH surface temperatures. Therefore, reducing the uncertainty of NA carbon uptake in ESMs will reduce uncertainty in future NH surface warming, and consequently in future global warming. Although the Southern Ocean accounts for 40% of the global ocean's carbon uptake and hosts robust meridional overturning circulation[12,39–42], there is a large model uncertainty of simulated future carbon uptake in CMIP6 ESMs[19,29], which is not well correlated to the future projected NH surface temperatures (Supplementary Fig. 1).

Strong link between carbon uptake and present-day salinity

The strength of the AMOC determines the NA carbon uptake because it regulates the poleward transport of carbon-rich and warm subtropical

water to the sinking region[15,37]. Since April 2004, a direct measurement of the AMOC has been collected at 26° N[43], but the overlapping period between the CMIP6 historical period and the direct observations is only 10 years (2005–2014), which is not long enough to discern a global warming signal from natural interdecadal variability; thus, it may not be appropriate to use the AMOC as an emergent constraint for the projected warming.

AMOC intensity is closely related to SSS and SST in the NA subpolar region[44,45], but the SSS has a stronger intermodel correlation with the AMOC than that of the SST[44] (Extended Data Fig. 3). The SSS is related to the subduction of carbon-enriched surface waters to the deep ocean through oceanic deep convection[46,47]. In addition, the SSS is associated with carbon uptake because it modulates the solubility pump. More specifically, a high SSS is linked to an increase in dissolved inorganic carbon concentration, and thus to a reduction in carbon uptake[48], which is also confirmed in CMIP6 ESMs during the present-day climate (Supplementary Fig. 2). Therefore, SSS in the NA subpolar region (outlined in Fig. 1a) is a good indicator of AMOC intensity as well as the carbon uptake; thus, it is a suitable constraint based on a long-term period of reliable observational record.

Nevertheless, it is still necessary to consider the complexity of SSS and SST related to AMOC intensity, to avoid a simplification using the SSS[49]. First of all, the cumulative NA carbon uptake increases with GHG concentration under the SSP5–8.5 scenario in all ESMs. This implies that the ocean is able to absorb carbon from the atmosphere by the end of the twenty-first century without saturation (Extended Data Fig. 4). The present-day cumulative NA carbon uptake is highly correlated with the present-day SSS in the NA subpolar region (Fig. 3a). This implies that ESMs with a stronger AMOC tend to take up more carbon in the NA during the present-day, consistent with the notion that the intensity of ocean circulation determines the amount of carbon uptake[14]. Furthermore, it is found that the global heat–carbon coupling parameter (α) (Methods) is significantly correlated with the SSS in the NA subpolar region during the present-day (Extended Data Fig. 5). This suggests that we cannot exclude the possibility that the global ocean circulation also plays a role in determining the carbon uptake in the NA.

ESMs tend to simulate a lower SSS in the NA subpolar region in the future climate than that in the present-day (Fig. 3b), consistent with a decline in AMOC intensity from the present-day to the future climate. The intermodel distribution of present-day SSS in the NA subpolar region is highly correlated with that of the future climate ($r = 0.60$). Given that the SSS is an indicator of AMOC intensity in ESMs, this result implies that ESMs with higher SSS in the present-day (that is, strong AMOC) tend to simulate higher SSS in the NA subpolar region (that is, strong AMOC) in the future climate. Furthermore, there is a statistically significant positive intermodel relationship between the future SSS in the NA subpolar region and the future cumulative carbon uptake in the NA ($r = 0.69$) (Fig. 3c). Therefore, ESMs with higher SSS in the NA subpolar region (that is, strong AMOC) in the present-day climate tend to simulate a larger future cumulative NA carbon uptake (Fig. 3b,c).

Figure 3a–c also indicates that AMOC intensity, represented by the SSS in the NA subpolar region, is closely associated with the intermodel spread of cumulative carbon uptake in ESMs, both in the present-day and the future climate. Since the build-up of carbon is concentrated in the surface water through the air–sea carbon exchange, a poleward transport of carbon-enriched surface water and its penetration into deep ocean through the AMOC contributes to the amount of carbon uptake in the present-day and the future climate[14]. Indeed, the cumulative amount of carbon uptake at the end of the twenty-first century is highly correlated with that in the present-day (Supplementary Fig. 3), indicating that ESMs with an initially large uptake of carbon continue to take up more carbon in the future. Thus, ESMs with a high SSS in the NA subpolar region during the present-day tend to take up more carbon in the present-day (Fig. 3a) and this tendency will continue, leading to a larger uptake of carbon in the future (Fig. 3c). Consequently,
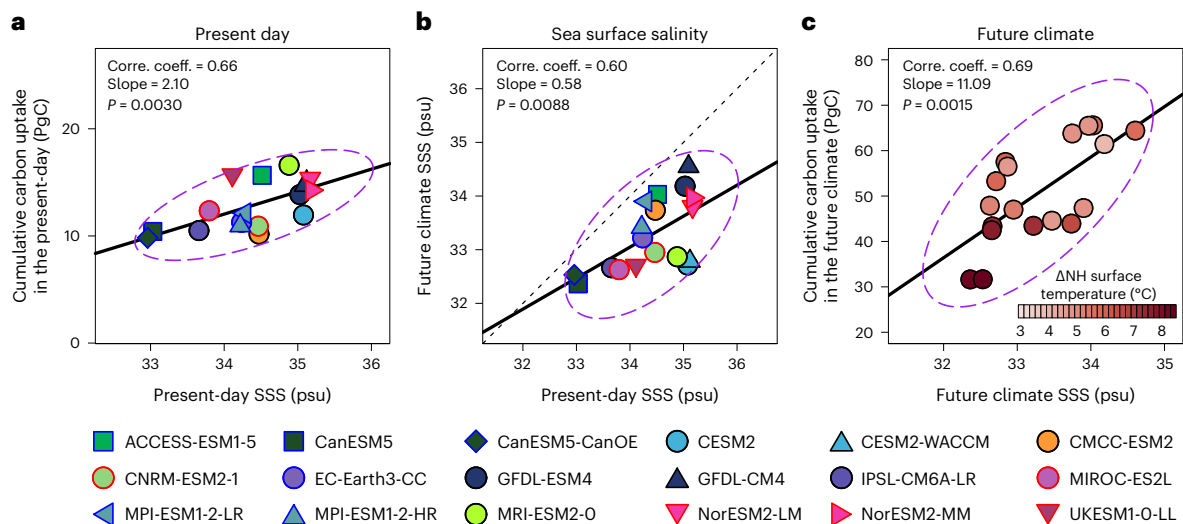
Fig. 3 | Intermodel difference in cumulative carbon uptake in the NA and SSS in the NA subpolar region. a, Simulated present-day cumulative carbon uptake in the NA versus present-day SSS in the NA subpolar region for 18 CMIP6 ESMs. **b**, Future climate of SSS in the NA subpolar region under the SSP5–8.5 scenario versus that in the present-day climate. The marker, which is on the lower side of the 1:1 line, indicates that the present-day SSS is higher than the future SSS in ESMs. **c**, Future cumulative carbon uptake in the NA versus future SSS in the NA subpolar region. Shadings indicate the corresponding changes of surface temperature in the NH. The purple dashed ellipse is calculated based on the multivariate normal distribution with 5–95% ranges. Correlation coefficient (Corre. coeff.), slope and P value determined by a two-sided Student's t-test are also provided with a regression line (black solid line).

the present-day SSS in the NA subpolar region is a key indicator of the amount of NA carbon uptake in the future. The changes in the amount of NA carbon uptake are associated with the future NH surface warming rate because an NA carbon uptake suppresses the greenhouse effect, and vice versa (Fig. 2). A similar conclusion is arrived on the causal link between SSS, the AMOC and NH warming, based on a composited analysis of two groups, one with higher and the other with lower present-day SSS in the NA subpolar region (Extended Data Fig. 6).

Reducing uncertainties in future NH surface warming

Climate model bias of the present-day SSS in the NA subpolar region could increase uncertainty in the future NH surface warming since it influences the amount of cumulative carbon uptake in the NA. Here we apply an emergent constraint to reduce the uncertainty in future NH surface warming based on the robust relationship between the present-day SSS in the NA subpolar region and the amount of cumulative NA carbon uptake.

The present-day SSS in the NA subpolar region has a strong negative correlation ($r = -0.72$) with future changes in NH surface temperature, and a strong positive correlation ($r = 0.88$) with cumulative carbon uptake in the NA (Fig. 4a,b). The observed SSS in the NA subpolar region and its uncertainty during 1981–2010, as obtained from the World Ocean Atlas 2018 (WOA18)[50], is estimated to be 34.75 ± 0.04 practical salinity unit (psu, Methods). This value is similar to that obtained from the CMIP6 ESMs mean of 34.41 ± 0.70 psu. The emergent relationship constrains the uncertainty in future projections of the NH surface warming and cumulative NA carbon uptake. We assume that all ESMs are independent by using only one ensemble member from each ESM, although some ESMs share the same key physical components and codes[51].

The constrained probability density functions are derived from the conditional probability density functions of the emergent relationship and the observed SSS in the NA subpolar region (Methods). After incorporating the emergent constraint based on the observed SSS (Methods), the NH surface temperature warming is reduced from 5.9 ± 1.4 °C to 5.5 ± 1.0 °C (Fig. 4c) and the cumulative NA carbon uptake is increased from 50.1 ± 10.7 PgC to 54.7 ± 5.1 PgC under SSP5–8.5

(Fig. 4d). The uncertainties in future NH warming and cumulative carbon uptake are reduced by 30% and 53%, respectively.

Since carbon uptake in the NA alters global atmospheric CO_2 concentration, it will also directly impact the future changes in global mean surface temperature. Therefore, there exists a strong relationship between the present-day SSS in the NA subpolar region and future global mean surface temperature changes in ESMs, with a significant negative correlation ($r = -0.64$) between the two. After incorporating the emergent constraints, the future global mean surface temperature is reduced from 4.7 °C ± 1.1 °C (before constraint) to 4.4 °C ± 0.8 °C (after constraint) with a 23% reduction in the uncertainty (Extended Data Fig. 7). This suggests that the projected global warming in the current ESMs is probably overestimated. To provide further evidence of the proposed emerging constraint, we conducted out-of-sample testing in CMIP5 ESMs[22,52]. Results support the proposed emerging constraint, reducing the uncertainty in the NH surface warming by 39% and in the cumulative NA carbon uptake by 26% (Extended Data Fig. 8).

The present-day AMOC strength during 2005–2014 as an emergent constraint results in a negative correlation with future NH surface temperature warming ($r = -0.63$) (Supplementary Fig. 4), which is lower than that using the SSS ($r = -0.72$ in Fig. 4a). NH warming is increased from 5.9 °C to 6.1 °C after the constraint, which is largely because the multimodel ensemble mean of AMOC intensity (17.4 sverdrups (Sv)) is stronger than the observed AMOC intensity (16.8 Sv). As mentioned above, the large variability and short duration of the observed AMOC lead to limitations of the AMOC-based constraint.

Discussion

We found that higher present-day SSS in the NA subpolar region, indicating stronger AMOC intensity, is associated with a larger amount of cumulative carbon uptake under global warming. This finding can be used to reduce the intermodel uncertainty in future changes in NH surface warming and cumulative carbon uptake. This constraint reduces intermodel uncertainty of future NH warming and NA carbon uptake by about 30% and 50%, respectively, under the SSP5–8.5 scenario (Fig. 4).

Current ESMs tend to underestimate the present-day SSS in the NA (Fig. 4a). Thus, the projected warming in NH is likely to be overestimated in the current ESMs, while the cumulative carbon uptake in
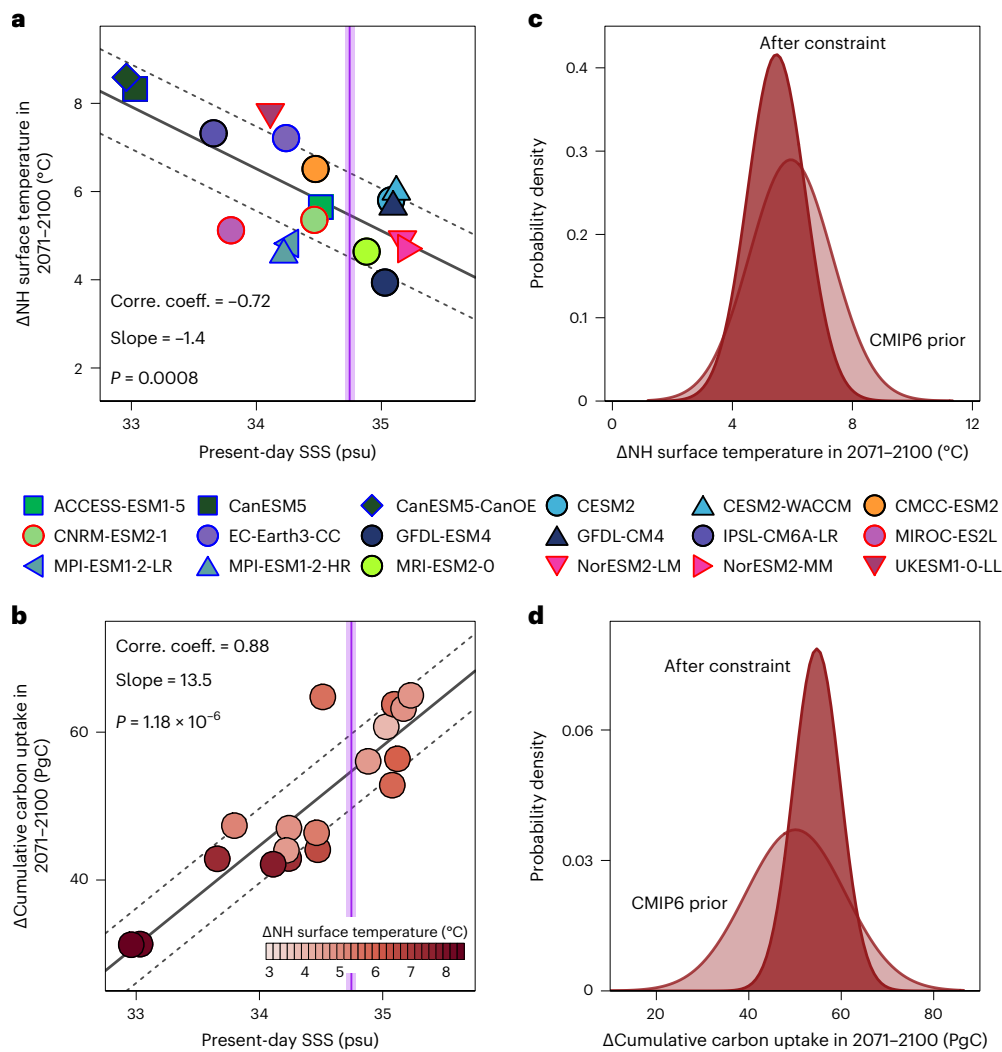
Fig. 4 | Emergent constraints on NH surface warming and NA cumulative carbon uptake. a,b, Projected changes in NH surface temperature (**a**) and cumulative carbon uptake in the NA (**b**) under the SSP5–8.5 scenario versus SSS in the NA subpolar region in the present-day climate (1981–2010). The solid black line follows the linear regression of 18 CMIP6 models, while the dashed black lines indicate prediction errors with one s.d. (and 68% confidence intervals). The solid vertical purple line (shading) indicates the climatology (one standard error) of the WOA18. The slope and *P* value in Fig. 4a,b are obtained by a two-sided Student's *t*-test. Shadings in **b** indicate the corresponding surface temperature change in the NH. **c,d**, Probability density functions for the projected NH surface warming (**c**) and cumulative carbon uptake changes in the NA (**d**) before ('CMIP6 prior', transparent) and after ('after constraint', opaque) when the emergent constraint is applied.

NA is underestimated (Fig. 4c,d). Furthermore, we reached a similar conclusion using a low emission scenario with SSP1–2.6 in which the emergent relationship between the present-day SSS in the NA subpolar region and future NH warming is statistically significant (Supplementary Fig. 5). Our results also suggest that SSS in the NA subpolar region is a constraint on projected global warming rates. Therefore, sustained observations of SSS in the NA subpolar region are beneficial for an accurate projection of the global warming rate in the future. In addition, the emergent relationship between the present-day SSS and future NH warming is much stronger in the 18 CMIP6 ESMs that include the ocean biogeochemical model component (*r* = −0.72 in Fig. 4a) compared with that in the other 22 CMIP6 ESMs without that component (*r* = −0.53 in Supplementary Fig. 6). Therefore, it is essential to use ESMs with a carbon cycle to reduce the uncertainty in future NH and global warming.

Online content

Any methods, additional references, Nature Portfolio reporting summaries, source data, extended data, supplementary information, acknowledgements, peer review information; details of author contributions

and competing interests; and statements of data and code availability are available at https://doi.org/10.1038/s41558-023-01728-y.

References

1. Bonnet, R. et al. Increased risk of near term global warming due to a recent AMOC weakening. *Nat. Commun.* **12**, 6108 (2021).
2. Latif, M., Sun, J., Visbeck, M. & Hadi Bordbar, M. Natural variability has dominated Atlantic Meridional Overturning Circulation since 1900. *Nat. Clim. Change* **12**, 455–460 (2022).
3. Rugenstein, M. A. A., Winton, M., Stouffer, R. J., Griffies, S. M. & Hallberg, R. Northern high-latitude heat budget decomposition and transient warming. *J. Clim.* **26**, 609–621 (2013).
4. Liu, W., Xie, S. P., Liu, Z. Y. & Zhu, J. Overlooked possibility of a collapsed Atlantic Meridional Overturning Circulation in warming climate. *Sci. Adv.* **3**, e1601666 (2017).
5. Keil, P. et al. Multiple drivers of the North Atlantic warming hole. *Nat. Clim. Change* **10**, 667–671 (2020).

6. Bellomo, K., Angeloni, M., Corti, S. & von Hardenberg, J. Future climate change shaped by inter-model differences in Atlantic Meridional Overturning Circulation response. *Nat. Commun.* **12**, 3659 (2021).

7. Liu, W., Fedorov, A. V., Xie, S. P. & Hu, S. N. Climate impacts of a weakened Atlantic Meridional Overturning Circulation in a warming climate. *Sci. Adv.* **6**, eaaz4876 (2020).

8. Frierson, D. M. W. et al. Contribution of ocean overturning circulation to tropical rainfall peak in the Northern Hemisphere. *Nat. Geosci.* **6**, 940–944 (2013).

9. Buckley, M. W. & Marshall, J. Observations, inferences, and mechanisms of the Atlantic Meridional Overturning Circulation: a review. *Rev. Geophys.* **54**, 5–63 (2016).

10. Gruber, N. et al. The oceanic sink for anthropogenic CO_2 from 1994 to 2007. *Science* **363**, 1193–1199 (2019).

11. Khatiwala, S. et al. Global ocean storage of anthropogenic carbon. *Biogeosciences* **10**, 2169–2191 (2013).

12. Sabine, C. L. et al. The oceanic sink for anthropogenic CO_2. *Science* **305**, 367–371 (2004).

13. Li, H., Ilyina, T., Müller, W. A. & Sienz, F. Decadal predictions of the North Atlantic CO_2 uptake. *Nat. Commun.* **7**, 11076 (2016).

14. Brown, P. J. et al. Circulation-driven variability of Atlantic anthropogenic carbon transports and uptake. *Nat. Geosci.* **14**, 571–577 (2021).

15. Pérez, F. F. et al. Atlantic Ocean CO_2 uptake reduced by weakening of the meridional overturning circulation. *Nat. Geosci.* **6**, 146–152 (2013).

16. Friedlingstein, P. et al. Global carbon budget 2020. *Earth Syst. Sci. Data* **12**, 3269–3340 (2020).

17. Cox, P. M., Betts, R. A., Jones, C. D., Spall, S. A. & Totterdell, I. J. Acceleration of global warming due to carbon-cycle feedbacks in a coupled climate model. *Nature* **408**, 184–187 (2000).

18. Matthews, H. D., Gillett, N. P., Stott, P. A. & Zickfeld, K. The proportionality of global warming to cumulative carbon emissions. *Nature* **459**, 829–832 (2009).

19. Frölicher, T. L. et al. Dominance of the Southern Ocean in anthropogenic carbon and heat uptake in CMIP5 models. *J. Clim.* **28**, 862–886 (2015).

20. Goris, N. et al. Constraining projection-based estimates of the future North Atlantic carbon uptake. *J. Clim.* **31**, 3959–3978 (2018).

21. Weijer, W., Cheng, W., Garuba, O. A., Hu, A. & Nadiga, B. T. CMIP6 models predict significant 21st century decline of the Atlantic Meridional Overturning Circulation. *Geophys. Res. Lett.* **47**, e2019GL086075 (2020).

22. Hall, A., Cox, P., Huntingford, C. & Klein, S. Progressing emergent constraints on future climate change. *Nat. Clim. Change* **9**, 269–278 (2019).

23. Dakos, V. et al. Slowing down as an early warning signal for abrupt climate change. *Proc. Natl Acad. Sci. USA* **105**, 14308–14312 (2008).

24. Shiogama, H., Watanabe, M., Kim, H. & Hirota, N. Emergent constraints on future precipitation changes. *Nature* **602**, 612–616 (2022).

25. Thackeray, C. W., Hall, A., Norris, J. & Chen, D. Constraining the increased frequency of global precipitation extremes under warming. *Nat. Clim. Change* **12**, 441–448 (2022).

26. Burger, F. A., Terhaar, J. & Frölicher, T. L. Compound marine heatwaves and ocean acidity extremes. *Nat. Commun.* **13**, 4722 (2022).

27. Thackeray, C. W. & Hall, A. An emergent constraint on future Arctic sea-ice albedo feedback. *Nat. Clim. Change* **9**, 972–978 (2019).

28. Cox, P. M., Huntingford, C. & Williamson, M. S. Emergent constraint on equilibrium climate sensitivity from global temperature variability. *Nature* **553**, 319–322 (2018).

29. Terhaar, J., Frölicher, T. L. & Joos, F. Southern Ocean anthropogenic carbon sink constrained by sea surface salinity. *Sci. Adv.* **7**, eabd5964 (2021).

30. Terhaar, J., Kwiatkowski, L. & Bopp, L. Emergent constraint on Arctic Ocean acidification in the twenty-first century. *Nature* **582**, 379–383 (2020).

31. Bourgeois, T., Goris, N., Schwinger, J. & Tjiputra, J. F. Stratification constrains future heat and carbon uptake in the Southern Ocean between 30°S and 55°S. *Nat. Commun.* **13**, 340 (2022).

32. Rahmstorf, S. Ocean circulation and climate during the past 120,000 years. *Nature* **419**, 207–214 (2002).

33. Haskins, R. K., Oliver, K. I. C., Jackson, L. C., Wood, R. A. & Drijfhout, S. S. Temperature domination of AMOC weakening due to freshwater hosing in two GCMs. *Clim. Dynam.* **54**, 273–286 (2020).

34. Holliday, N. P. et al. Ocean circulation causes the largest freshening event for 120 years in eastern subpolar North Atlantic. *Nat. Commun.* **11**, 585 (2020).

35. Caesar, L., Rahmstorf, S. & Feulner, G. On the relationship between Atlantic Meridional Overturning Circulation slowdown and global surface warming. *Environ. Res. Lett.* **15**, 024003 (2020).

36. Chemke, R., Zanna, L. & Polvani, L. M. Identifying a human signal in the North Atlantic warming hole. *Nat. Commun.* **11**, 1540 (2020).

37. Sarmiento, J. L., Gruber, N., Brzezinski, M. A. & Dunne, J. P. High-latitude controls of thermocline nutrients and low latitude biological productivity. *Nature* **427**, 56–60 (2004).

38. Borchert, L. F. et al. Improved decadal predictions of North Atlantic subpolar gyre SST in CMIP6. *Geophys. Res. Lett.* **48**, e2020GL091307 (2021).

39. Friedlingstein, P. et al. Global carbon budget 2022. *Earth Syst. Sci. Data* **14**, 4811–4900 (2022).

40. Gruber, N. et al. Oceanic sources, sinks, and transport of atmospheric CO_2. *Global Biogeochem. Cycles* https://doi.org/10.1029/2008GB003349 (2009).

41. Chen, C. L., Liu, W. & Wang, G. H. Understanding the uncertainty in the 21st century dynamic sea level projections: the role of the AMOC. *Geophys. Res. Lett.* **46**, 210–217 (2019).

42. Zhang, L., Delworth, T. L. & Zeng, F. The impact of multidecadal Atlantic Meridional Overturning Circulation variations on the Southern Ocean. *Clim. Dynam.* **48**, 2065–2085 (2017).

43. Cunningham, S. A. et al. Temporal variability of the Atlantic Meridional Overturning Circulation at 26°N. *Science* **317**, 935–938 (2007).

44. Caesar, L., Rahmstorf, S., Robinson, A., Feulner, G. & Saba, V. Observed fingerprint of a weakening Atlantic Ocean overturning circulation. *Nature* **556**, 191–196 (2018).

45. Rahmstorf, S. et al. Exceptional twentieth-century slowdown in Atlantic Ocean overturning circulation. *Nat. Clim. Change* **5**, 475–480 (2015).

46. Broecker, W. S. & Peng, T.-H. Interhemispheric transport of carbon dioxide by ocean circulation. *Nature* **356**, 587–589 (1992).

47. Cheng, W., Chiang, J. C. H. & Zhang, D. X. Atlantic Meridional Overturning Circulation (AMOC) in CMIP5 models: RCP and historical simulations. *J. Clim.* **26**, 7187–7197 (2013).

48. Dore, J. E., Lukas, R., Sadler, D. W. & Karl, D. M. Climate-driven changes to the atmospheric CO_2 sink in the subtropical North Pacific Ocean. *Nature* **424**, 754–757 (2003).

49. Menary, M. B. et al. Aerosol-forced AMOC changes in CMIP6 historical simulations. *Geophys. Res. Lett.* **47**, e2020GL088166 (2020).

50. Zweng, M. et al. *World Ocean Atlas 2018, Vol. 2: Salinity*. NOAA Atlas NESDIS 82 (A. Mishonov Technical Editor, 2019); https://archimer.ifremer.fr/doc/00651/76339/

51. Schlund, M., Lauer, A., Gentine, P., Sherwood, S. C. & Eyring, V. Emergent constraints on equilibrium climate sensitivity in CMIP5: do they hold for CMIP6? *Earth Syst. Dynam.* **11**, 1233–1258 (2020).

52. Brunner, L. et al. Reduced global warming from CMIP6 projections when weighting models by performance and independence. *Earth Syst. Dynam.* **11**, 995–1012 (2020).

Publisher's note Springer Nature remains neutral with regard to jurisdictional claims in published maps and institutional affiliations.

Methods

CMIP5 and CMIP6 models

We used 31 ESMs based on CMIP6 (18 models) and CMIP5 (13 models); see detail in Extended Data Table 1 (refs. [53],[54]). ESMs with coupled ocean biogeochemistry schemes were applied within the context of both climate and ocean biogeochemical projections[55],[56]. All model simulations cover the period 1850 to 2100 (1861–2100 for GFDL-ESM2G and GFDL-ESM2M, 1860–2100 for HadGEM2-CC) following historical forcing changes, including GHG, aerosols and natural variation over the period 1850–2005 (CMIP5) or 1850–2014 (CMIP6). CMIP6 models follow SSP5–8.5 simulations of the future (2015–2100). For CMIP5 models, the simulations follow the Representative Concentration Pathway 8.5 for 2006–2100.

Statistical methods for emergent relationship

We used a total least squares (TLS) method to fit a linear regression and a multivariate probability distribution function (PDF) to obtain the uncertainty range. TLS regression minimizes the perpendicular distances between the CMIP6 data points and the regression line. Therefore, the errors between the independent and dependent variables are uncorrelated. The multivariate PDF is a joint probability distribution of the data points, taking into account the relationships between all variables in the dataset to find the most likely distribution. This difference between TLS regression and multivariate PDF results in an asymmetric relationship between the regression line and the uncertainty range.

Global heat–carbon coupling parameter

We calculated the oceanic anthropogenic carbon storage (C_{ant}) by vertically integrating the dissolved inorganic carbon throughout the historical simulation[19]. Global ocean heat storage (H) is calculated from the potential temperature of each grid cell. Temperature is converted to ocean heat storage by vertical integration through each model level and multiplied by a fixed value for density and heat capacity of 4.15×10^6 kg m^{-3} J K^{-1}. Heat and carbon storage anomalies are calculated with respect to a pre-industrial control simulation to avoid the influence of climate drift. There is a linear correlation between the two variables, similar to the relationship between atmospheric warming and cumulative carbon emissions[57]. The global heat–carbon coupling parameter (α) is derived from a regression of anthropogenic ocean carbon storage (C_{ant}) onto the ocean heat storage (H):

$$\alpha = \frac{\int H(x,y,t)\mathrm{d}A}{\int C_{ant}(x,y,t)\mathrm{d}A} = \frac{\hat{H}(t)}{\hat{C}_{ant}(t)} \tag{1}$$

$\hat{H}$ and $\hat{C}_{ant}$ are globally integrated values and A is the surface grid area. x, y and t are longitude, latitude and time. The value of α is generally in the range of 4.2×10^7 to 8.6×10^7 J mol^{-1}.

Emergent constraint

PDFs of projected NH warming and carbon uptake in the NA were calculated following a previously established methodology[58]. The emergent relationship in this study was a linear regression of CMIP6 models between the simulated present-day state, x (surface salinity), and projected changes, y (NH surface temperature and cumulative carbon uptake in the NA), in the future (2071–2100). We used an ordinary least squares regression for linear regression and only one ensemble from each model for equal model weighting. The prior PDF assumed models followed a Gaussian distribution. The PDFs of observational constraints were defined as:

$$P(x) = \frac{1}{\sqrt{2\pi\sigma_x^2}} \exp\left\{-\frac{(x-\bar{x})^2}{2\sigma_x^2}\right\} \tag{2}$$

where $\bar{x}$ is the average of the observed surface salinity in the North Atlantic subpolar region for 1981–2010 (present-day) and σ_x is the corresponding standard error. The 'prediction error' of the emergent multimodel linear regression ($\sigma_f(x)$) defines contours of equal probability density around the multimodel linear regression, which represent the probability density of y given x:

$$P\{y|x\} = \frac{1}{\sqrt{2\pi\sigma_f^2}} \exp\left\{-\frac{(y-f(x))^2}{2\sigma_f^2}\right\} \tag{3}$$

where $f(x)$ is the fitted value of the linear regression and σ_f is the prediction error of the linear regression. The emergent relationship was combined with the observational PDF by calculating the product of their PDFs and then integrating across the x-axis variable to derive a constrained PDF:

$$P(y) = \int_{-\infty}^{\infty} P\{y|x\} P(x)\, \mathrm{d}x \tag{4}$$

AMOC stream function

The stream function of the AMOC was calculated from the Atlantic Ocean meridional velocity $v(x,y,z,t)$ of climate model outputs based on longitude (x), latitude (y), depth (z) and time (t) as:

$$\Psi_A(y,z,t) = \int_z^H \int_{X_{west}}^{X_{east}} v(x,y,z,t)\, \mathrm{d}x\mathrm{d}z \tag{5}$$

where H is the sea bottom and X_{west} and X_{east} are the boundary. The AMOC stream function, Ψ_A, is measured in sverdrups (1 Sv = 10^6 m^3 s^{-1}). If models provided the stream function variable ('msftmz' and 'msftyz'), we calculated the AMOC based on these data. The AMOC index was defined as the maximum of the AMOC stream function at a latitude of 26° N below 50 m, based on the observational monitoring standard in the Rapid Climate Change Meridional Overturning Circulation Heat-flux Array[59].

Cumulative ocean carbon uptake

Anthropogenic air–sea CO_2 flux was the difference between the air–sea CO_2 flux ('fgco2') in historical simulations merged with future simulations and concurrent pre-industrial control (piControl) experiments. This definition of anthropogenic air–sea CO_2 flux includes both the flux driven by increasing atmospheric CO_2 concentrations and any flux from changes in the natural air–sea CO_2 flux due to internal climate variability and climate change, such as changes in ocean circulation, wind conditions and primary production driven by anthropogenic and natural forcings[29],[31].

SSS and the Atlantic subpolar region

For observations, version 2 of the WOA18 annual climatology (1981–2010) of salinity was used for the observation-based constraint. The confidence interval of the observations was calculated from standard errors during the present-day. All output fields were analysed on a horizontal 1° × 1° interpolated model grid. The North Atlantic subpolar region is defined as 55° W–15° W and 45° N–65° N and the Northern Hemisphere is defined as 0–360° E and 10° N–90° N. The observed SSS in the NA subpolar region obtained from Multi Observation Global Ocean Sea Surface Salinity and Sea Surface Density[60] was also analysed and its uncertainty during 1993–2014 was estimated as 34.78 ± 0.05 psu (Supplementary Fig. 4).

Intermodel uncertainty

One s.d. of the changes among ESMs is defined as an intermodel uncertainty. For Fig. 1a,b, shadings illustrate the signal of future climate

changes by multimodel mean and contours illustrate the uncertainty of future climate changes by one s.d. among CMIP6 ESMs.

Data availability

All data, CMIP5 and CMIP6 outputs are available from the ESGF portals (https://esgf-node.llnl.gov). The WOA18 salinity climatology and standard error are available from the National Oceanographic Data Center portal at https://www.ncei.noaa.gov/access/world-ocean-atlas-2018. Multi Observation Global Ocean Sea Surface Salinity and Sea Surface Density is available at https://data.marine.copernicus.eu/product/MULTIOBS_GLO_PHY_S_SURFACE_MYNRT_015_013/description. Rapid Climate Change Meridional Overturning Circulation Heat-flux Array for the observational AMOC is available at https://rapid.ac.uk/ or https://climate.metoffice.cloud/amoc.html#datasets. The data necessary to reproduce the results are available at https://doi.org/10.5281/zenodo.7948570 (ref. 61).

Code availability

All plots and analysis were carried out using NCAR Command Language v.6.6.2. To interpolate the model grid data, we used climate data operators available at https://code.mpimet.mpg.de/projects/cdo/. The codes for generating the figures in this work are available at https://doi.org/10.5281/zenodo.7948570 (ref. 61).

References

53. Eyring, V. et al. Overview of the Coupled Model Intercomparison Project Phase 6 (CMIP6) experimental design and organization. *Geosci. Model Dev.* **9**, 1937–1958 (2016).
54. Taylor, K. E., Stouffer, R. J. & Meehl, G. A. An overview of CMIP5 and the experiment design. *Bull. Am. Meteorol. Soc.* **93**, 485–498 (2012).
55. Bopp, L. et al. Multiple stressors of ocean ecosystems in the 21st century: projections with CMIP5 models. *Biogeosciences* **10**, 6225–6245 (2013).
56. Kwiatkowski, L. et al. Twenty-first century ocean warming, acidification, deoxygenation, and upper-ocean nutrient and primary production decline from CMIP6 model projections. *Biogeosciences* **17**, 3439–3470 (2020).
57. Bronselaer, B. & Zanna, L. Heat and carbon coupling reveals ocean warming due to circulation changes. *Nature* **584**, 227–233 (2020).
58. Cox, P. M. et al. Sensitivity of tropical carbon to climate change constrained by carbon dioxide variability. *Nature* **494**, 341–344 (2013).
59. Moat, B. et al. Atlantic Meridional Overturning Circulation observed by the RAPID-MOCHA-WBTS (RAPID-Meridional Overturning Circulation and Heatflux Array-Western Boundary Time Series) array at 26N from 2004 to 2020 (v.2020.2). *NERC EDS British Oceanographic Data Centre NOC* https://doi.org/10.5285/e91b10af-6f0a-7fa7-e053-6c86abc05a09 (2022).
60. Droghei, R., Nardelli, B. B. & Santoleri, R. A new global sea surface salinity and density dataset from multivariate observations (1993–2016). *Front. Mar. Sci.* https://doi.org/10.3389/fmars.2018.00084 (2018).
61. Park, I.-H. et al. North Atlantic salinity constrains Northern Hemisphere and global warming codes related to main figures. *Zenodo* https://doi.org/10.5281/zenodo.7948570 (2023).
62. Ziehn, T. et al. The Australian Earth System Model: ACCESS-ESM1.5. *J. South. Hemisph. Earth Syst. Sci.* **70**, 193–214 (2020).
63. Swart, N. C. et al. The Canadian Earth System Model version 5 (CanESM5.0.3). *Geosci. Model Dev.* **12**, 4823–4873 (2019).
64. Gent, P. R. et al. The Community Climate System Model version 4. *J. Clim.* **24**, 4973–4991 (2011).
65. Danabasoglu, G. et al. The Community Earth System Model version 2 (CESM2). *J. Adv. Model. Earth. Syst.* **12**, e2019MS001916 (2020).
66. Fogli, P. G. & Iovino, D. CMCC–CESM–NEMO: toward the new CMCC Earth system model. *Centro Euro-Mediterraneo sui Cambiamenti Climatici* https://www.cmcc.it/wp-content/uploads/2015/02/rp0248-ans-12-2014.pdf (2014).
67. Cherchi, A. et al. Global mean climate and main patterns of variability in the CMCC-CM2 coupled model. *J. Adv. Model. Earth Syst.* **11**, 185–209 (2019).
68. Voldoire, A. et al. Evaluation of CMIP6 DECK experiments with CNRM-CM6-1. *J. Adv. Model. Earth Syst.* **11**, 2177–2213 (2019).
69. Döscher, R. et al. The EC-Earth3 Earth system model for the Coupled Model Intercomparison Project 6. *Geosci. Model Dev.* https://doi.org/10.5194/gmd-15-2973-2022 (2021).
70. Dunne, J. P. et al. GFDL's ESM2 global coupled climate–carbon Earth system models. Part I: physical formulation and baseline simulation characteristics. *J. Clim.* **25**, 6646–6665 (2012).
71. Held, I. M. et al. Structure and performance of GFDL's CM4.0 climate model. *J. Adv. Model. Earth Syst.* **11**, 3691–3727 (2019).
72. Schmidt, G. A. et al. Configuration and assessment of the GISS ModelE2 contributions to the CMIP5 archive. *J. Adv. Model. Earth Syst.* **6**, 141–184 (2014).
73. Collins, W. J. et al. Development and evaluation of an Earth-System Model – HadGEM2. *Geosci. Model Dev.* **4**, 1051–1075 (2011).
74. Sellar, A. A. et al. Implementation of UK Earth system models for CMIP6. *J. Adv. Model. Earth Syst.* **12**, e2019MS001946 (2020).
75. Dufresne, J. L. et al. Climate change projections using the IPSL-CM5 Earth system model: from CMIP3 to CMIP5. *Clim. Dynam.* **40**, 2123–2165 (2013).
76. Boucher, O. et al. Presentation and evaluation of the IPSL-CM6A-LR climate model. *J. Adv. Model. Earth Syst.* **12**, e2019MS002010 (2020).
77. Watanabe, S. et al. MIROC-ESM 2010: model description and basic results of CMIP5-20c3m experiments. *Geosci. Model Dev.* **4**, 845–872 (2011).
78. Hajima, T. et al. Development of the MIROC-ES2L Earth system model and the evaluation of biogeochemical processes and feedbacks. *Geosci. Model Dev.* **13**, 2197–2244 (2020).
79. Giorgetta, M. A. et al. Climate and carbon cycle changes from 1850 to 2100 in MPI-ESM simulations for the Coupled Model Intercomparison Project phase 5. *J. Adv. Model. Earth Syst.* **5**, 572–597 (2013).
80. Mauritsen, T. et al. Developments in the MPI-M Earth System Model version 1.2 (MPI-ESM1.2) and its response to increasing CO_2. *J. Adv. Model. Earth Syst.* **11**, 998–1038 (2019).
81. Yukimoto, S. et al. The Meteorological Research Institute Earth System Model version 2.0, MRI-ESM2.0: description and basic evaluation of the physical component. *J. Meteorol. Soc. Japan* **97**, 931–965 (2019).
82. Seland, O. et al. Overview of the Norwegian Earth System Model (NorESM2) and key climate response of CMIP6 DECK, historical, and scenario simulations. *Geosci. Model Dev.* **13**, 6165–6200 (2020).

Acknowledgements

Author contributions

I.-H.P. and S.-W.Y. contributed equally to designing the research. I.-H.P. performed the data analysis and, together with S.-W.Y., interpreted the results. I.-H.P. wrote the manuscript and edited it together with S.-W.Y. All the authors discussed the study results and reviewed the manuscript.

Competing interests

The authors declare no competing interests.

Additional information

Extended data is available for this paper at https://doi.org/10.1038/s41558-023-01728-y.

Supplementary information The online version contains supplementary material available at https://doi.org/10.1038/s41558-023-01728-y.

Correspondence and requests for materials should be addressed to Sang-Wook Yeh.

Peer review information *Nature Climate Change* thanks Leonard Borchert and the other, anonymous, reviewer(s) for their contribution to the peer review of this work.

Reprints and permissions information is available at www.nature.com/reprints.

Extended Data Table 1 | CMIP5 and CMIP6 models used in this study and the corresponding model centre

| Model name	Modelling centre
ACCESS-ESM1-5 (ref. 62)	The Commonwealth Scientific and Industrial Research Organisation (Australia)
CanESM5 (ref. 63)	Canadian Centre for Climate Modelling and Analysis (Canada)
CanESM5-CanOE[63]	
CESM1-BGC[64]	National Center for Atmospheric Research, Climate and National Center for Atmospheric Research, Climate and Global Dynamics Laboratory, (USA)
CESM2 (ref. 65)	
CESM2-WACCM[65]	
CMCC-CESM[66]	Fondazione Centro Euro-Mediterraneo sui Cambiamenti Climatici (Italy)
CMCC-ESM2 (ref. 67)	
CNRM-ESM2-1 (ref. 68)	Centre National de Recherches Météorologiques (France)
EC-Earth3-CC[69]	EC-Earth consortium, Rossby Center, Swedish Meteorological and Hydrological Institute/SMHI (Sweden)
GFDL-ESM2G[70]	National Oceanic and Atmospheric Administration, Geophysical Fluid Dynamics Laboratory (US)
GFDL-ESM2M[70]	
GFDL-CM4 (ref. 71)	
GFDL-ESM4 (ref. 71)	
GISS-E2-H-CC[72]	Goddard Institute for Space Studies, National Aeronautics and Space Administration (US)
GISS-E2-R-CC[72]	
HadGEM2-CC[73]	Met Office Hadley Centre (UK)
UKESM1-0-LL[74]	
IPSL-CM5A-LR[75]	Institut Pierre-Simon Laplace (France)
IPSL-CM5A-MR[75]	
IPSL-CM6A-LR[76]	
MIROC-ESM[77]	Japan Agency for Marine-Earth Science and Technology (Japan)
MIROC-ESM-CHEM[77]	
MIROC-ES2L[78]	
MPI-ESM-LR[79]	Max Planck Institute for Meteorology (Germany)
MPI-ESM-MR[79]	
MPI-ESM1-2-LR[80]	
MPI-ESM1-2-HR[80]	
MRI-ESM2-O (ref. 81)	Meteorological Research Institute (Japan)
NorESM2-LM[82]	Climate modeling Consortium consisting of Center for International Climate and Environmental Research (Norway)
NorESM2-MM[82]	

CMIP5 models are in italics.
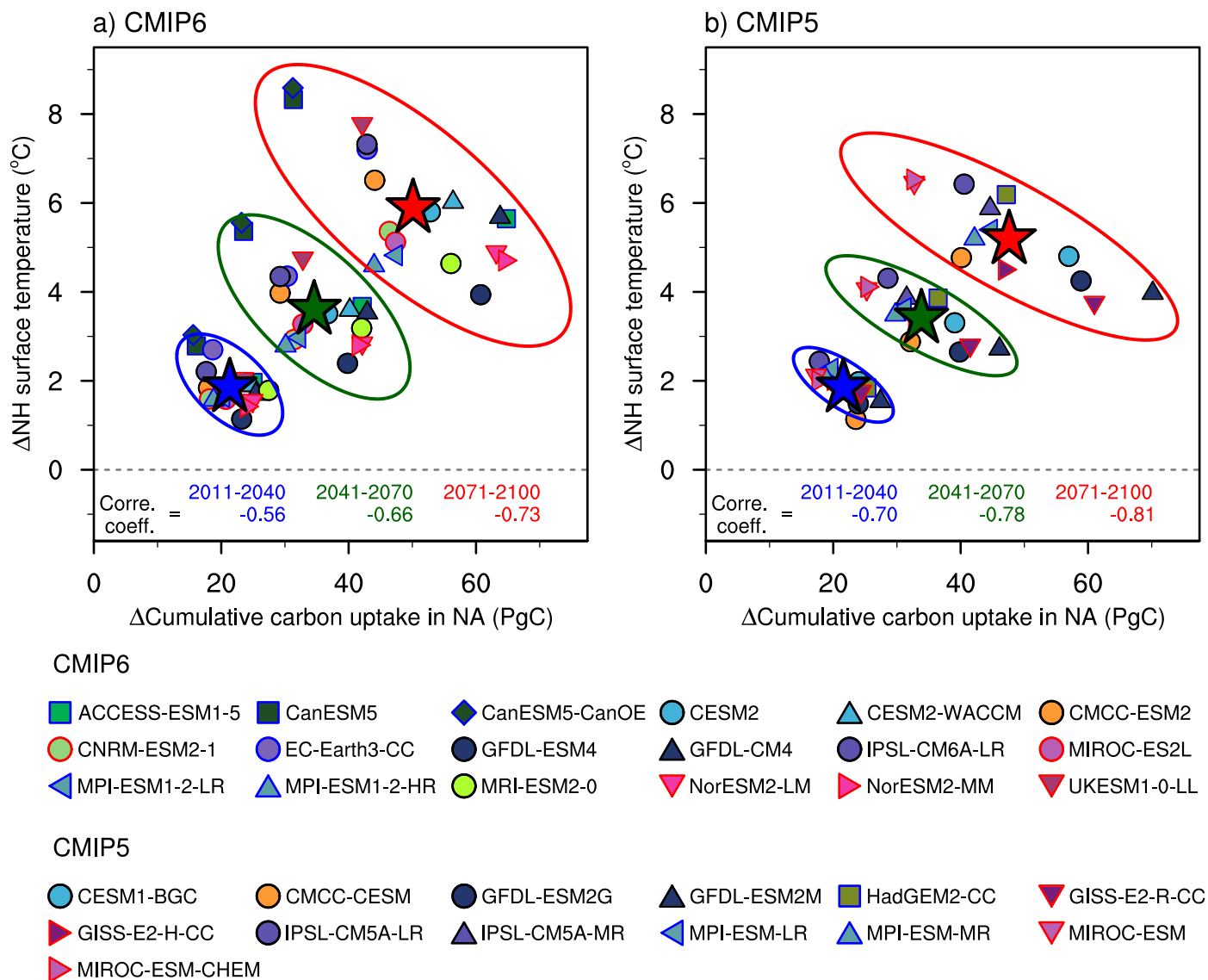
Extended Data Fig. 1 | Future surface temperature changes in the Northern Hemisphere (NH) linked to projected cumulative carbon uptake in the North Atlantic (NA). a, **b**, The inter-model relationship between projected changes in the NH surface temperature and carbon uptake in the NA from a, CMIP6 and b, CMIP5. Ellipses of different colours are calculated based on the multivariate normal distribution with 5–95% ranges of different 30-year periods (blue: 2011–2040, green: 2041–2070, red: 2071–2100). Stars indicate multi-model means of the ESMs.
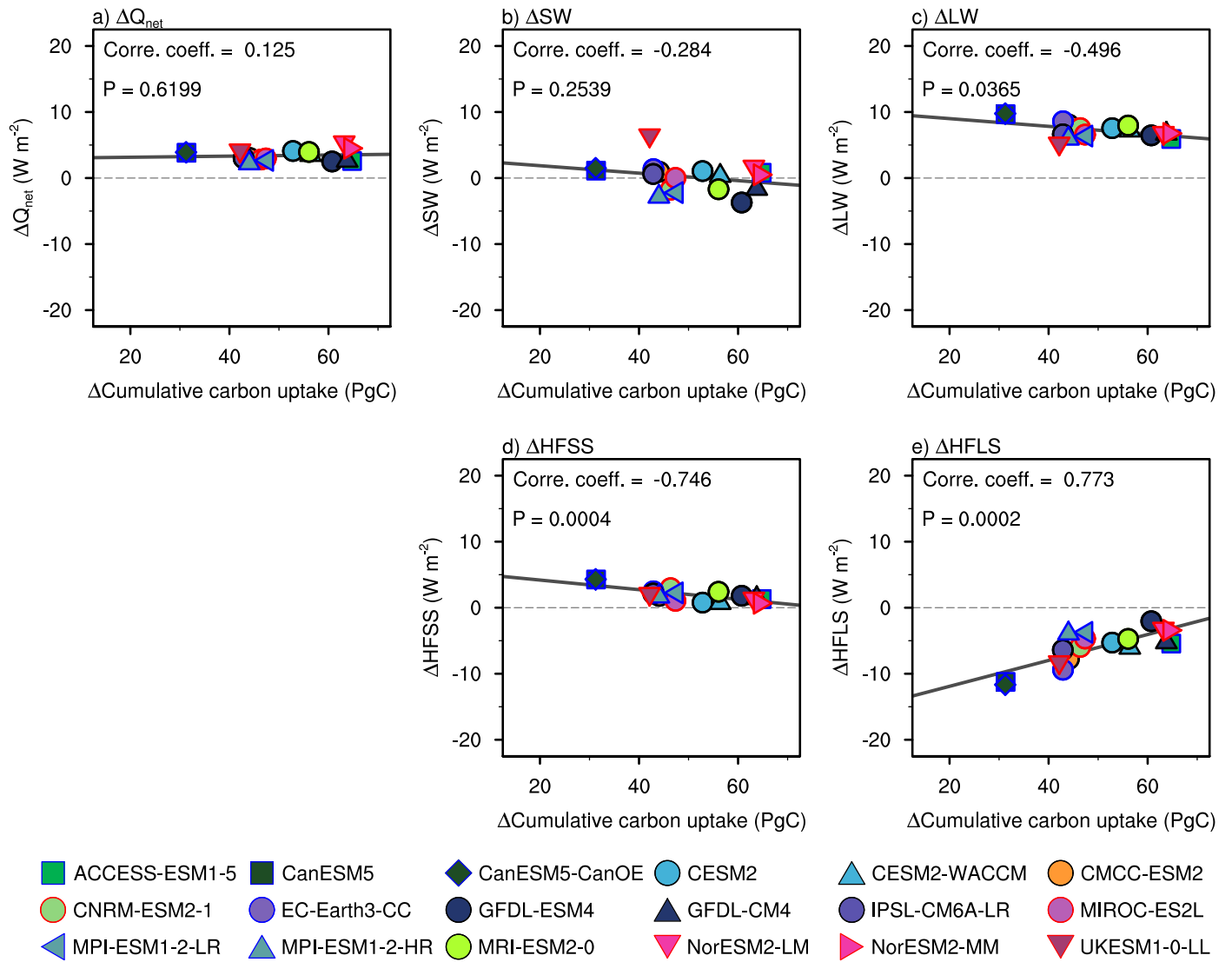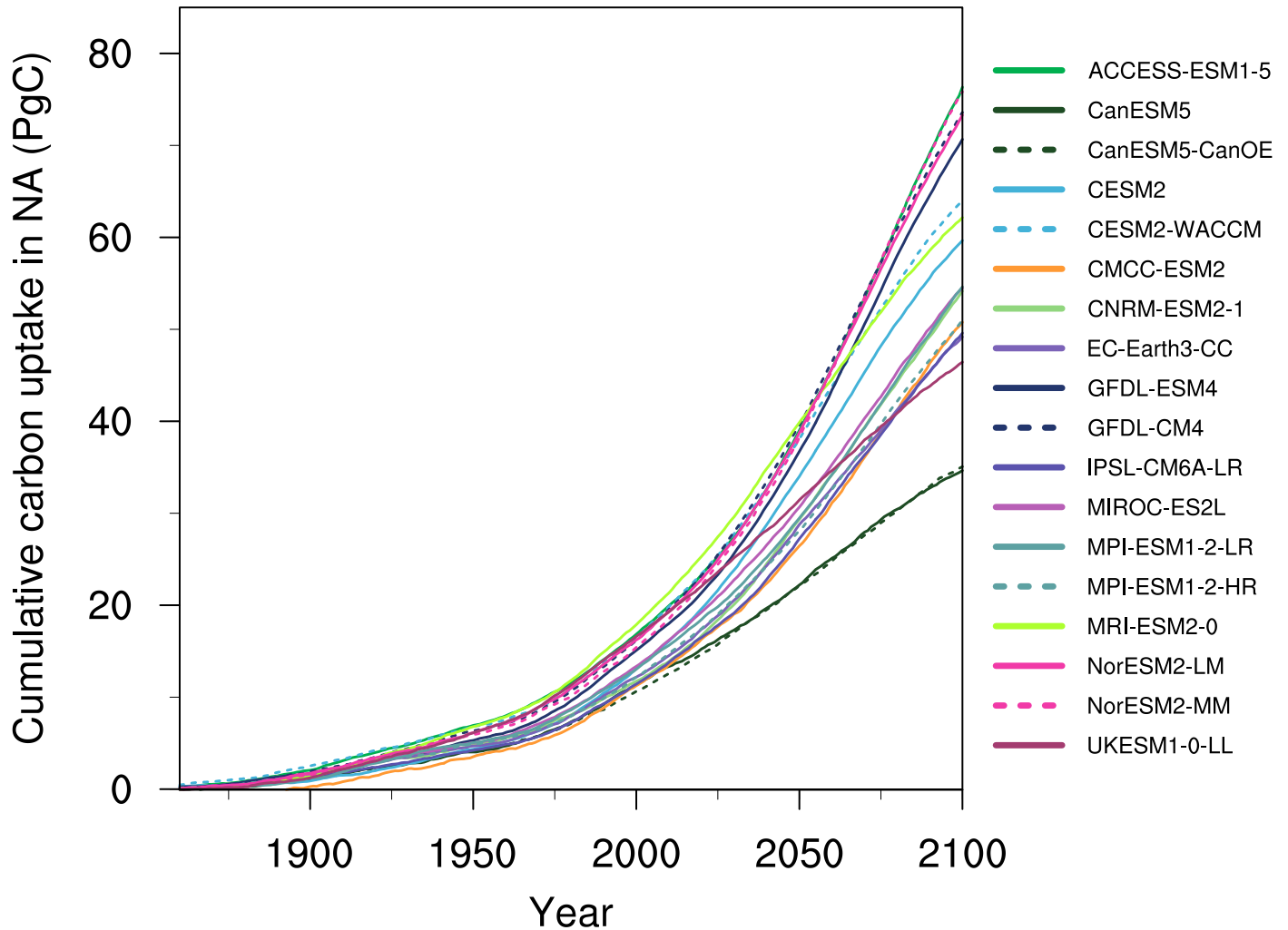
Extended Data Fig. 2 | Inter-model difference between future surface heat flux in the Northern Hemisphere and future cumulative carbon uptake in the North Atlantic. a, Projected change total net heat flux (Qnet) in the Northern Hemisphere and cumulative carbon uptake in the North Atlantic. **b**–**e**, The same as a but for net surface shortwave radiation (SW), net surface longwave radiation (LW), sensible heat flux (HFSS), and latent heat flux (HFLS).
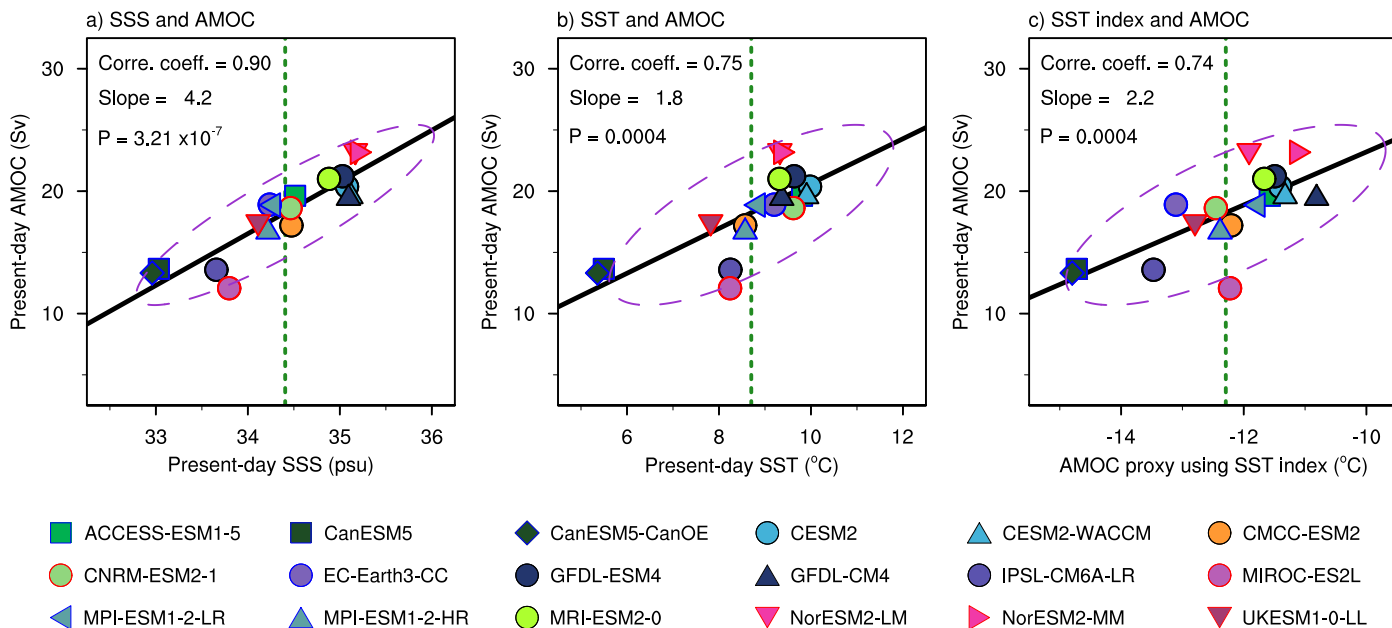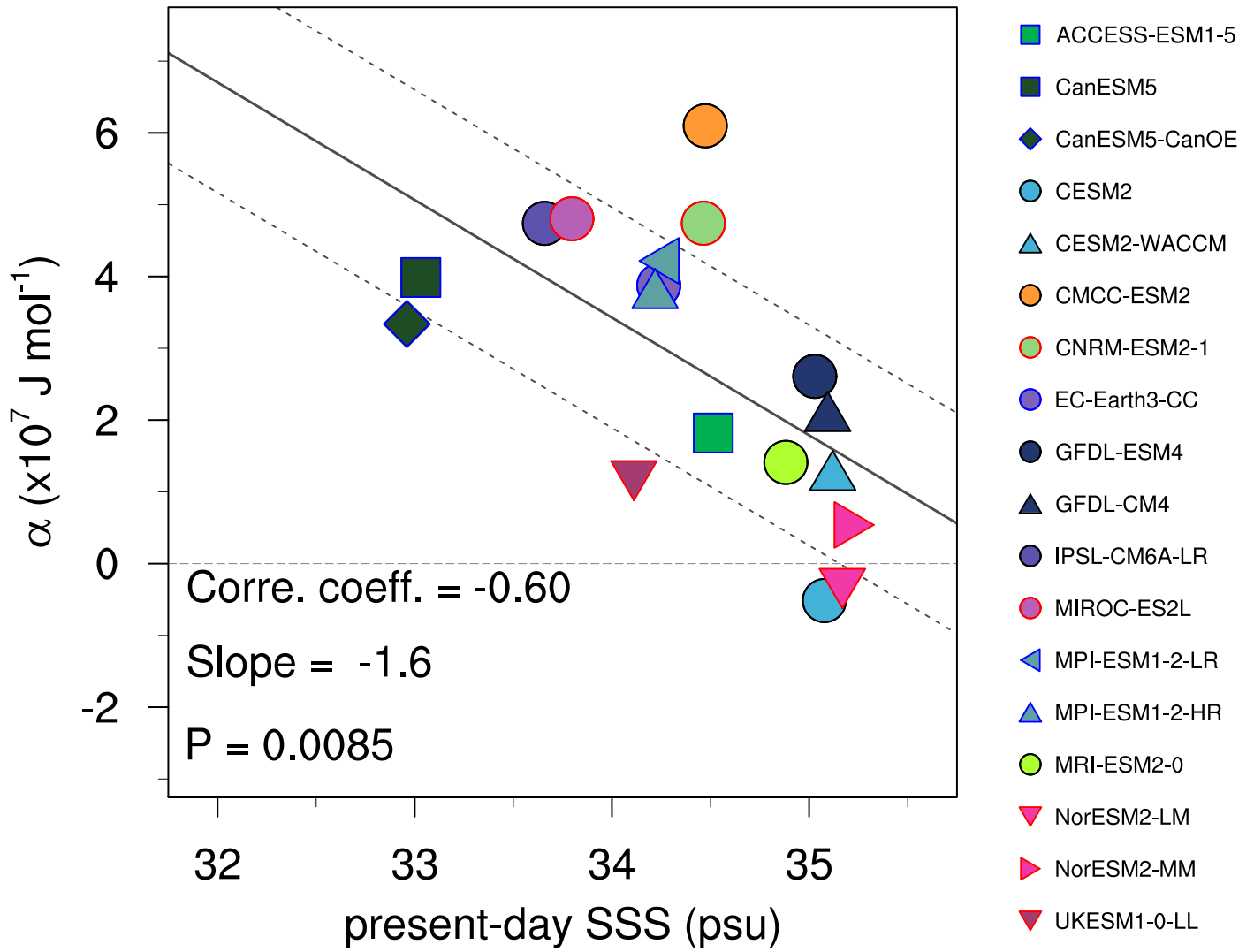
Extended Data Fig. 3 | Inter-model difference of present-day climate variables against the present-day AMOC in CMIP6 ESMs. a, Simulated present-day AMOC (Sv) versus sea surface salinity (SSS) and **b**, sea surface temperature (SST) in the North Atlantic subpolar region. **c**, AMOC proxy using the SST index versus present-day AMOC. The purple dashed ellipse is calculated based on the multivariate normal distribution with 5–95% ranges. Correlation coefficient (Corre. Coeff.), slope and P value determined by a two-sided Student's t-test are also provided with a regression line (black solid line). Vertical green dashed lines illustrate the multi-model means of ESMs.

Extended Data Fig. 4 | Projection of cumulative North Atlantic (NA) carbon uptake in CMIP6. ESMs projection of NA cumulative carbon uptake since 1850 from 18 CMIP6 ESMs under the SSP5-8.5 scenarios.

Extended Data Fig. 5 | Inter-model difference in global heat-carbon coupling parameter (α) versus sea surface salinity in the NA subpolar region during the present-day climate. The solid black line follows the linear regression of 18 CMIP6 ESMs, while the dashed black lines indicate prediction errors with one standard deviation (and 68% confidence intervals).
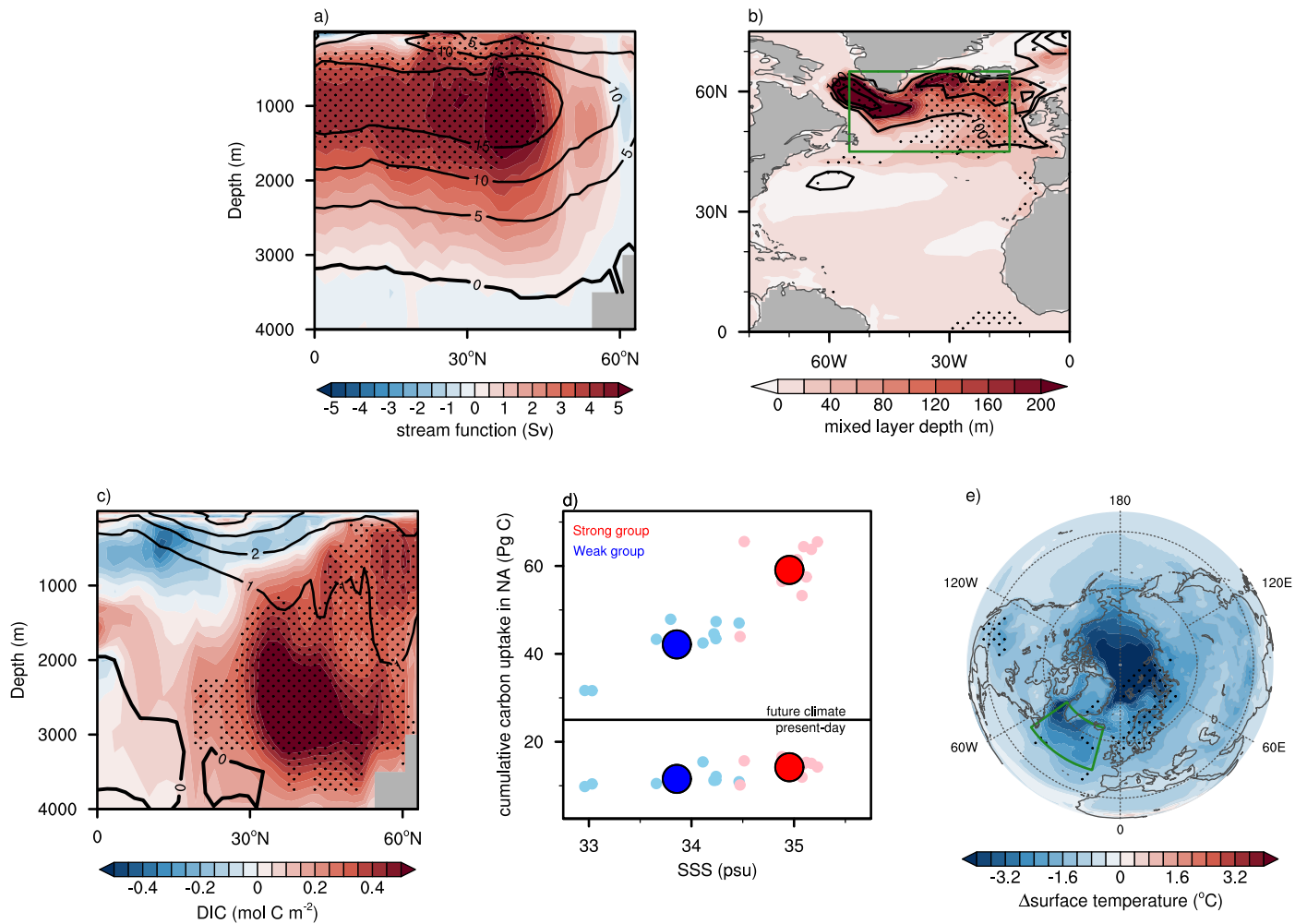
Extended Data Fig. 6 | Composite comparison between two groups. a–c, Differences between two groups (high sea surface salinity (SSS) minus low SSS in the NA subpolar region) in the present-day climate state (shading) of a, meridional streamfuction, b, mixed layer depth, c, zonal mean dissolved inorganic carbon. The two groups were divided into 9 CMIP6 ESMs based on the present-day SSS in the NA subpolar region. Contours illustrate the multi-model ensemble mean of 18 CMIP6 ESMs. Stipples indicate regions that are statistically significant at 99% confidence level by Student's t-test. Green box indicates NA subpolar region. **d,** Inter-model difference of SSS over the NA subpolar region in the present-day and cumulative carbon uptake in the NA for the present-day (bottom) and future climate (top). Light colors illustrate each ensemble and dark colors multi-model ensemble mean of each group. **e,** Difference between two groups in future changes (shading) of surface temperature.
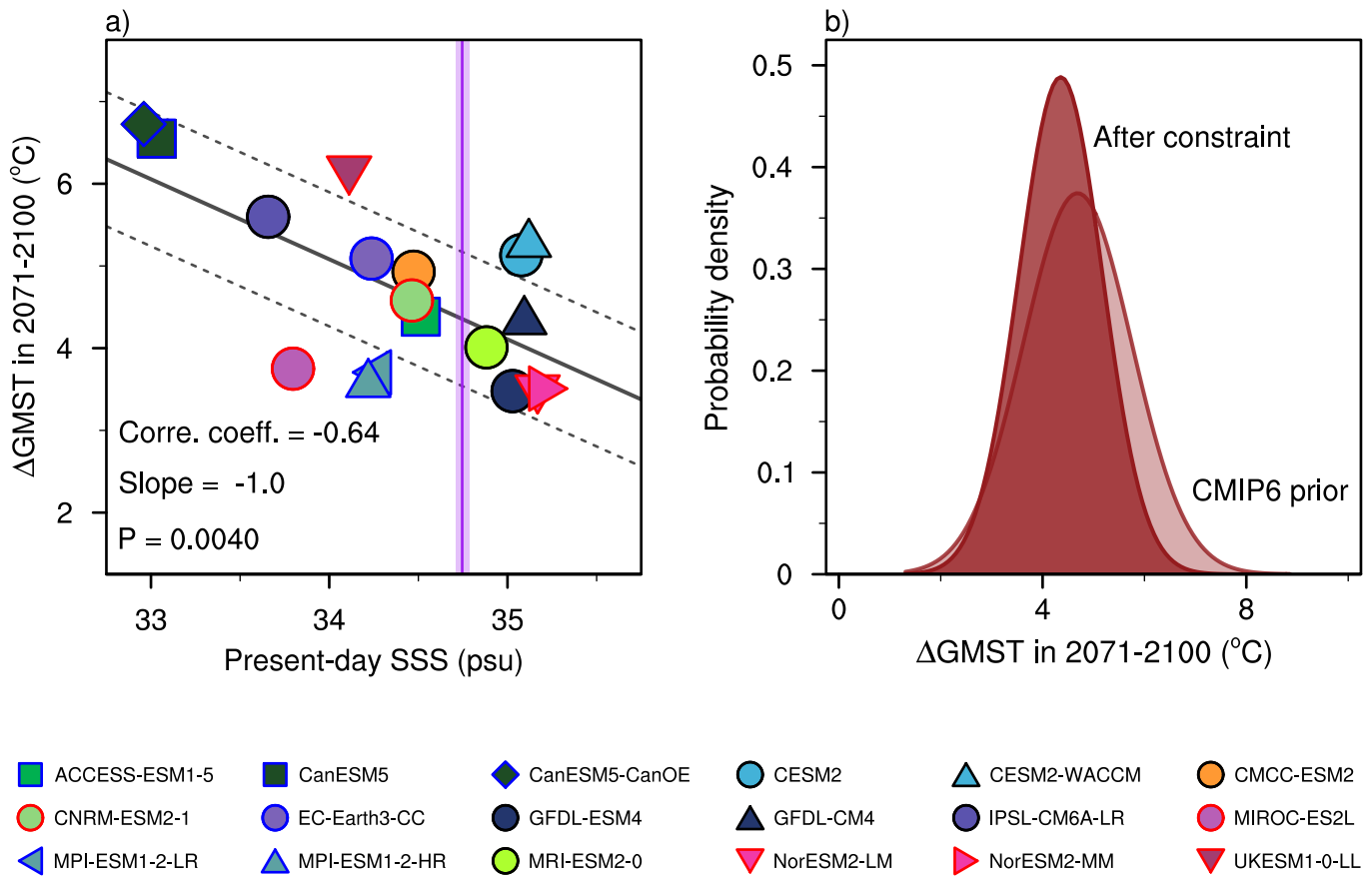
Extended Data Fig. 7 | Emergent constraints on the future global mean surface temperature (GMST). a, Projected changes in GMST under SSP5-8.5 scenario versus sea surface salinity (SSS) of the NA subpolar region in the present-day climate (1981–2010). The solid black line follows the linear regression of 18 CMIP6 ESMs, while the dashed black lines indicate prediction errors with one standard deviation (and 68% confidence intervals). A solid purple line (shading) indicates the climatology (one standard error) of the World Ocean Atlas 2018 with slope and p-value determined by a two-sided Student's t-test. **b**, Probability density functions for the projected GMST changes in the NA before ('CMIP6 prior', transparent) and after ('after constraint', opaque) when the emergent constraint is applied.
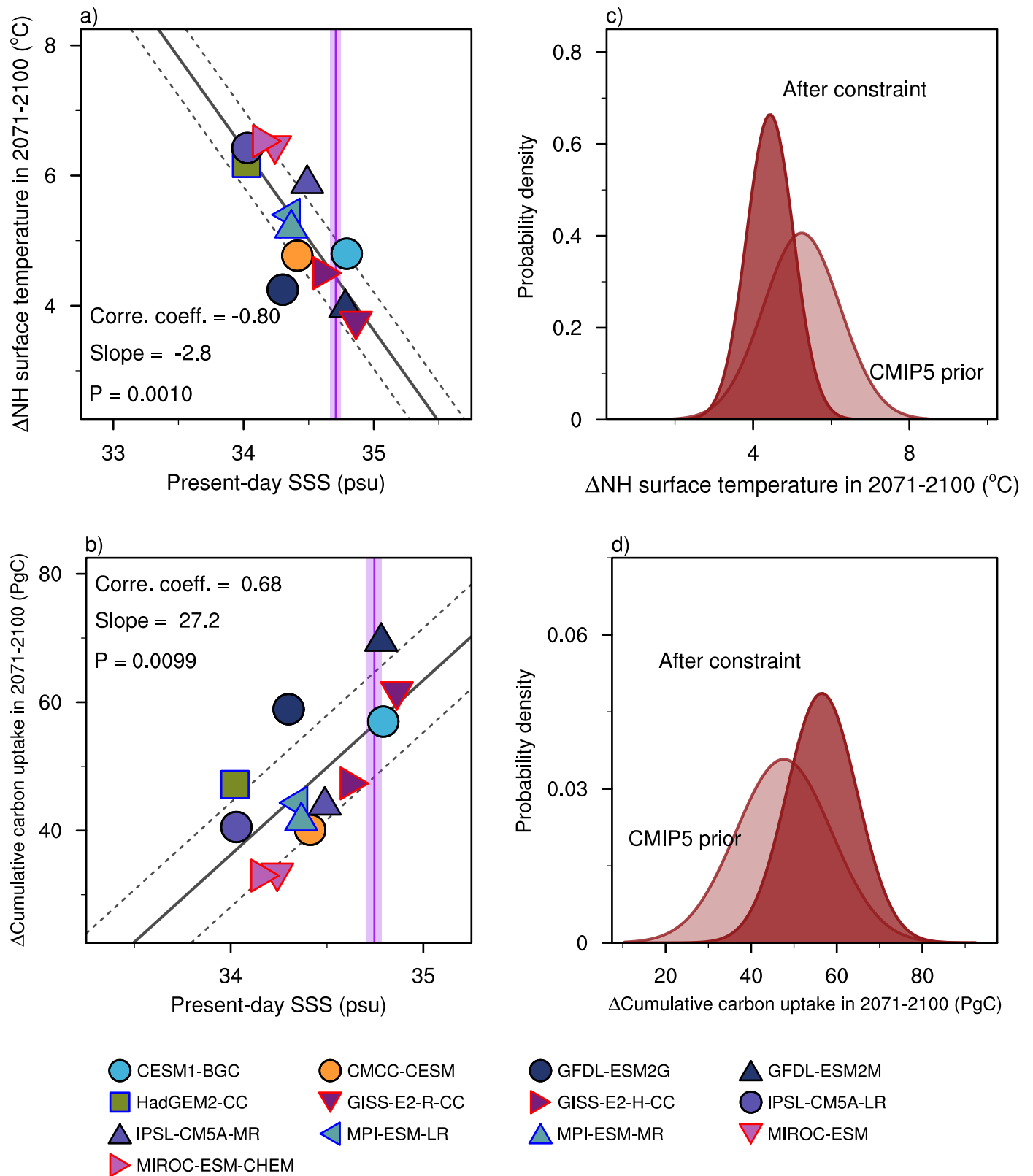
Extended Data Fig. 8 | Emergent constraints on the Northern Hemisphere (NH) surface warming and the North Atlantic (NA) cumulative carbon uptake in CMIP5 ESMs. a, Projected changes in NH surface temperature and b, cumulative carbon uptake in the NA under RCP8.5 scenario versus sea surface salinity (SSS) of the NA subpolar region in the present-day climate (1981–2010). The solid black line follows the linear regression of 13 CMIP5 ESMs, while the dashed black lines indicate prediction errors with one standard deviation (and 68% confidence intervals). A solid purple line (shading) indicates the climatology (one standard error) of the World Ocean Atlas 2018 with slope and p-value determined by a two-sided Student's t-test. c, Probability density functions for the projected NH surface warming and d, cumulative carbon uptake in the NA before ('CMIP5 prior', transparent) and after ('after constraint', opaque) when the emergent constraint is applied.